Letters

Implementation of Dual Three-Phase Linear Hall Sensor-Based Embedded Magnetic Encoder in Permanent Magnet Synchronous Motors

Chao Zhang, Yuchen Wang, Zheng Wu, Wei Hua, *Senior Member, IEEE*, and Meiwei Zhang

***Abstract*—Normally, three-phase linear Hall sensor-based embedded magnetic encoder (EME) are used in permanent magnet synchronous motors to detect the rotor angle, in which prefilters are used to suppress the harmonic disturbance. However, due to the employment of prefilters, this EME system shows large estimated angle error at low-speed regions and weak dynamic response performance. In this letter, a dual three-phase linear Hall sensor-based EME system is proposed with the help of the vector space decomposition method. It can effectively eliminate the harmonic interference without introducing prefilters and the accuracy of rotor angle estimation can be improved at all-speed regions, which is validated by experiments.**

***Index Terms*—Embedded magnetic encoder (EME), harmonics, permanent magnet synchronous motor (PMSM), vector space decomposition (VSD).**

I. Introduction

RECENTLY, owing to the advantages of low cost and space-saving, linear Hall sensor-based embedded magnetic encoder (EME) for permanent magnet synchronous motors (PMSMs) have been widely studied [1], [2], [3], [4], [5], [6], [7], [8]. In the EME system, as shown in Fig. 1, two or three linear Hall sensors are installed in the PMSM's cavity to sense the PM flux density (PMFD), and the linear Hall signals are used for the rotor's angle estimation. However, because the PMFD is always nonsinusoidal, the Hall voltage signals are always distorted by harmonic components (mainly 3rd, 5th, and 7th orders) [2], [3], [4], which results in harmonic error in the estimated rotor position.

Generally, prefilters can be cascaded before synchronous reference frame (SRF) phase-locked loop (PLL) or arctan operator

Manuscript received 5 April 2024; revised 5 May 2024; accepted 17 May 2024. Date of publication 24 May 2024; date of current version 16 July 2024. This work was supported in part by Postgraduate Research and Practice Innovation Program of Jiangsu Province under Grant KYCX24_0395, in part by Jiangsu Funding Program for Excellent Postdoctoral Talent under Grant 2023ZB430, and in part by the Jiangsu Provincial Key Laboratory of Smart Grid Technology and Equipment, Southeast University. *(Corresponding author: Wei Hua.)*

Chao Zhang, Zheng Wu, Wei Hua, and Meiwei Zhang are with the School of Electrical Engineering, Southeast University, Nanjing 210096, China (e-mail: 230238797@seu.edu.cn; wuzheng96@seu.edu.cn; huawei1978@seu.edu.cn; 101300260@seu.edu.cn).

Yuchen Wang is with the Department of Electronic & Electrical Engineering, University of Bath, Bath BA2 7AY, China (e-mail: wangyuchen1994@seu.edu.cn).

Color versions of one or more figures in this article are available at https://doi.org/10.1109/TPEL.2024.3404848.

Digital Object Identifier 10.1109/TPEL.2024.3404848

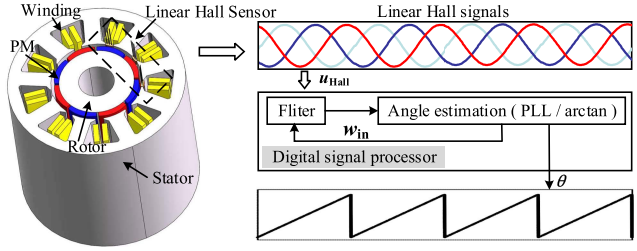

Fig. 1. Scheme of EME.

to eliminate the above harmonic error [3], [4], [5], as seen in Fig. 1. The adaptive notch filter [3] and the synchronous frequency extractor [4] can effectively eliminate the 3rd harmonic distortion from linear Hall signals but have no rejection ability over negative sequence harmonic components. In [5], the multiple-complex coefficient filter (MCCF) [9] is employed in the EME system to suppress multiple harmonic components. Besides, an improved differential type MCCF (DT-MCCF) is proposed to address the startup problem in the application of EME.

Although these filters can adaptively suppress specific harmonic components, limitations still exist when applying them in the EME system.

1) These filters behave low-pass characteristics for fundamental component, resulting in a reduced bandwidth of the angle calculation system and the dynamic performance, which is unfavorable for the angular feedback performance of the EME system [6].
2) When the frequency is low, these filters cannot accurately distinguish the fundamental component and harmonic components, so the harmonics rejection ability is weak at low-speed regions [5].

To address the aforementioned problems, this article innovatively uses the vector space decomposition (VSD) method [10], [11] to extract the fundamental frequency component and propose corresponding structures of the dual three-phase (DTP) EME system. Therefore, both the dynamic performance and accuracy of the angle estimation system can be improved without introducing a cumbersome prefilter.

The rest of this article is organized as follows. In Section II, the VSD method for DTP Hall signal is briefly introduced, followed by the analysis of the corresponding installation pattern of

DTP-EME. Then, the rotor angle decoding algorithm is formed. In Section III, comprehensive experiments are conducted to compare the performance between the proposed method and prefilter-based methods. Finally, Section IV concludes this article.

II. Implementation of DTP-EME

A. VSD for DTP Hall Signal

In the past, the VSD method was normally utilized for the decoupled analysis of DTP machines [10], in which the 6-D vector space describing the current/voltage vectors can be decomposed into three orthogonal subspaces, namely, $\alpha\beta$-subspace, $o1o2$-subspace, and xy-subspace (collectively called $\alpha\beta v$-space). After decomposition, the fundamental frequency component of the current/voltage was mapped into $\alpha\beta$-subspace to achieve electromechanical energy conversion.

Builds on the previous work, the VSD method is introduced in this article to separate harmonic disturbance of the linear Hall signals from a new perspective. First, the PMFD was sensed by six linear Hall sensors and output DTP Hall signal as described in (1) and (2). Among them [see (1)], u_{H1}, u_{H5}, and u_{H9} are symmetrically distributed by $2\pi/3$. The other group (u_{H2}, u_{H6}, u_{H10}) has similar characteristics with (u_{H1}, u_{H5}, u_{H9}) and the phase difference between u_{H1} and u_{H2} is $\pi/6$.

Then, the DTP Hall signal was described as 6-D vectors and transformed to $\alpha\beta v$-space by equations shown as (3)–(5). After transformation, the components at the fundamental frequency and $(12m\pm1)$th order ($m = 1,2,3\ldots$) harmonics are mapped into the $\alpha\beta$-subspace, as shown in (6). Other harmonics are transferred to the remaining two subspaces, which realize the effective separation from the fundamental component. Because the linear Hall output signals rarely have $(12m\pm1)$th order harmonic components, the processed orthogonal signals in $\alpha\beta$-subspace (u_α-u_β) are almost standard sine wave, which improves the accuracy of angle estimation.

$$\boldsymbol{u}_{\text{Hall}} = [u_{H1}\ u_{H2}\ u_{H5}\ u_{H6}\ u_{H9}\ u_{H10}]^T \tag{1}$$

$$u_{Hi} = \sum_{n=1,3,5\ldots} U_n \cos\left(n\left(\varphi - \frac{(i-1)\pi}{6}\right)\right)$$

$$i = 1,2,5,6,9,10 \tag{2}$$

$$\boldsymbol{u}_{\boldsymbol{\alpha\beta v}} = [T_{\text{VSD}}] \cdot \boldsymbol{u}_{\text{Hall}} \tag{3}$$

$$\boldsymbol{u}_{\boldsymbol{\alpha\beta v}} = [u_\alpha\ u_\beta\ u_{o1}\ u_{o2}\ u_x\ u_y]^T \tag{4}$$

$$[T_{\text{VSD}}] = \frac{1}{3}\begin{bmatrix} 1 & \frac{\sqrt{3}}{2} & -\frac{1}{2} & -\frac{\sqrt{3}}{2} & -\frac{1}{2} & 0 \\ 0 & \frac{1}{2} & \frac{\sqrt{3}}{2} & \frac{1}{2} & -\frac{\sqrt{3}}{2} & -1 \\ 1 & 0 & 1 & 0 & 1 & 0 \\ 0 & 1 & 0 & 1 & 0 & 1 \\ 1 & -\frac{\sqrt{3}}{2} & -\frac{1}{2} & \frac{\sqrt{3}}{2} & -\frac{1}{2} & 0 \\ 0 & \frac{1}{2} & -\frac{\sqrt{3}}{2} & \frac{1}{2} & \frac{\sqrt{3}}{2} & -1 \end{bmatrix} \tag{5}$$

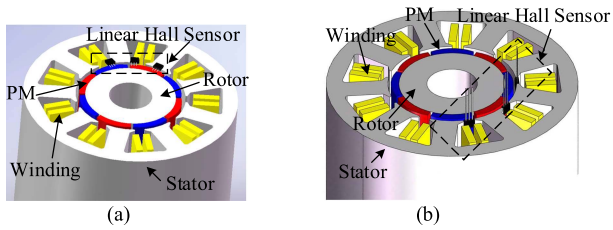

Fig. 2. Installation scheme of linear Hall sensors in EME system. (a) Pattern 1. (b) Pattern 2.

$$\begin{cases} u_\alpha = U_1\cos\theta + \sum_{m=1,2\ldots} & (U_{12m-1}\cos(12m-1)\theta + \\ & U_{12m+1}\cos(12m+1)\theta) \\ u_\beta = U_1\sin\theta + \sum_{m=1,2\ldots} & (-U_{12m-1}\sin(12m-1)\theta \\ & +U_{12m+1}\sin(12m+1)\theta). \end{cases} \tag{6}$$

B. Installation Scheme of DTP Linear Hall Sensors

Based on the analysis in Section II-A, to separate the harmonic components in the original linear Hall signals by the VSD method, six linear Hall sensors should be installed at intervals of $(6k\pm1)\pi/6$ ($k = 1,2$) elec. rad to obtain DTP Hall signal satisfying the specific phase difference as expressed in (1) and (2).

There are two typical locations of linear Hall sensors, i.e., end cover and stator slot, as seen in Fig. 2. To achieve the desired phase shift in the DTP linear Hall signal, the installation scheme of linear Hall sensors needs to be designed in the following two patterns.

Pattern 1: Linear Hall sensors are located at the end cover of PMSMs to detect the axial PMFD [1], [3], as seen in Fig. 2(a). The circumferential distance between the linear Hall sensors can be adjusted arbitrarily, so the installation scheme of linear Hall sensors with $(6k\pm1)\pi/6$ ($k = 1,2$) elec. rad phase shift can be always achieved.

Pattern 2: Linear Hall sensors are located at the stator slot openings to detect the radial PMFD [5], [6], as seen in Fig. 2(b). For a motor with N_s stator slots and N_r pole pairs, the circumferential angle α between adjacent stator slots can be expressed as (7). To meet the installation requirement of the DTP linear Hall sensors, the circumferential angle α is constrained by (8). Therefore, the installation scheme of linear Hall sensors with $(6k\pm1)\pi/6$ ($k = 1,2$) elec. rad phase shift can be achieved when the slot-pole combinations of the motor meet $(6k_1\pm1)N_s = 12k_2N_r$ ($k_1 = 0,1,2\ldots$, $k_2 = 1,2,3\ldots$).

$$\alpha = \frac{2N_r\pi}{N_s} \tag{7}$$

$$\alpha = \frac{2N_r\pi}{N_s} = \frac{(6k_1 \pm 1)\pi}{6k_2}\quad (k_1 = 0,1,2\ldots,\ k_2 = 1,2\ldots). \tag{8}$$

C. Angle Decoding Algorithm

The scheme of the angle decoding algorithm is organized as Fig. 3, which is composed of two parts: 1) VSD transformation

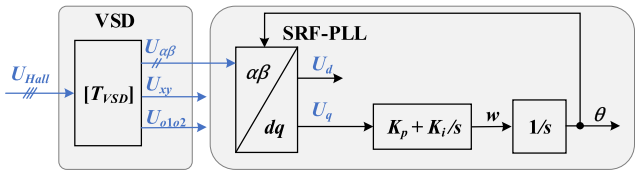

Fig. 3. Scheme of angle decoding algorithm based on VSD.

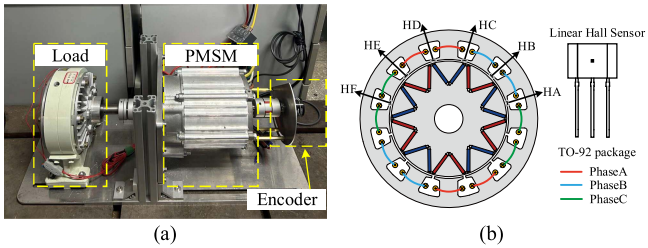

Fig. 4. (a) Experimental setup. (b) Installation position of six linear hall sensors.

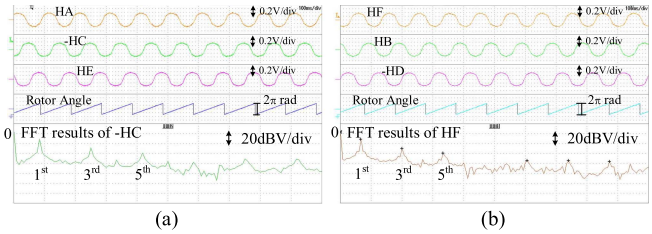

Fig. 5. (a) Signals of HA, -HC, HE, and FFT results of -HC. (b) Signals of HF, HB, -HD, and FFT results of HF. (-HC represents the inverse signal of HC, -HD represents the inverse signal of HD).

and 2) SRF-PLL. First, six linear Hall sensors are installed based on the installation scheme described in Section B and DTP Hall signals $\boldsymbol{u_{Hall}}$ [see (1) and (2)] are obtained. Then, $\boldsymbol{u}_{\text{Hall}}$ are delivered to VSD transformation module and the output two-phase orthogonal signals $\boldsymbol{U}_{\alpha\beta}$ are sent to SRF-PLL module. Subsequently, the SRF-PLL is used to estimate the angular frequency (w) and phase angle (θ) of $\boldsymbol{U}_{\alpha\beta}$. The overall system is called VSD-PLL, which can effectively eliminate the unfavorable harmonic components without adding any complicated prefilter, thus both the angle estimation accuracy and dynamic performance are improved.

III. Experiment Validation

To validate the proposed decoding algorithm, an experiment platform is set up, as shown in Fig. 4(a), where 12 slots/10 poles PMSM, an adjustable load, and an optical encoder are coaxially connected. In the PMSM, six linear Hall sensors HA-HF (Type: DRV5055-A4) are fixed at the central axis of stator slots to sense the radial flux density [shown in Fig. 4(b)].

A. Linear Hall Signals Under Open-Circuit Condition

The output signals of six linear Hall sensors are recorded in Fig. 5. It can be found that the signals from HA, -HC, and HE

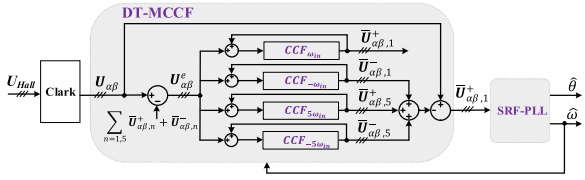

Fig. 6. Scheme of DTMCCF-PLL.

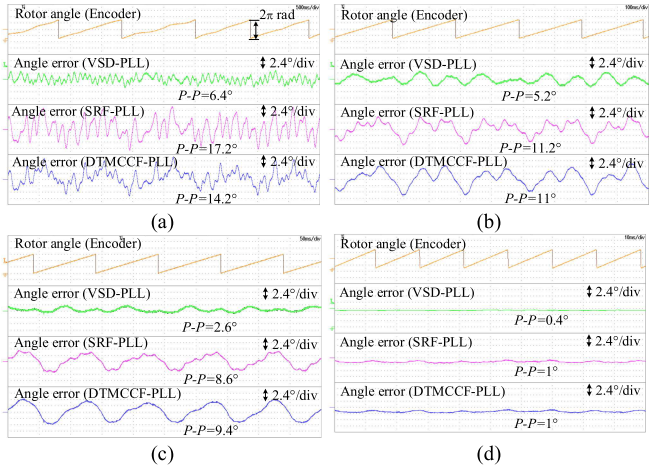

Fig. 7. Estimated angle error under different operation speeds: (a) 12, (b) 60, (c) 120, and (d) 1000 r/min.

are distributed by $2\pi/3$. The other group (HF, HB, -HD) has similar characteristics with (HA, -HC, HE), and the phase shift between HA and HF is $\pi/6$. The DTP Hall signals (HA, HF, -HC, HB, HE, -HD) satisfy the phase relationship of (1) and (2). As seen in Fig. 5, the Hall signals are contaminated by the amplitude/phase unbalance and harmonic components (mainly 3rd and 5th), which deteriorate the angle decoding accuracy.

B. Performance Comparisons Under Steady State

The motor is controlled by the field-oriented control (FOC) algorithm, in which the decoding angle/speed from the optical encoder is used as the angle/speed feedback module. Then, SRF-PLL, prefilter-based SRF-PLL (DTMCCF-PLL in [5]), and VSD-PLL are implemented under the same condition for comparison. The scheme of DTMCCF-PLL is shown in Fig. 6. To effectively suppress both amplitude/phase unbalance and 5th harmonic components, an applicable damping ratio k_c in DTMCCF is tuned to be 0.707. Besides, to guarantee both static performance and dynamic response of the PLL system, the parameters $K_p = 100$ and $K_i = 5000$ in the loop filter are a suitable choice for different operation conditions.

The rotor angle calculated by the optical encoder is used as a reference, the estimated angle error of the three methods under various speeds are depicted in Fig. 7 and Table I. At different speeds, VSD-PLL always shows the smallest angle error among these decoding algorithms. The fast Fourier transforms (FFTs) results of the angle error in Fig. 7 are shown in Fig. 8. Some findings can be summarized as follows.

TABLE I
ESTIMATED ANGLE ERROR UNDER VARIOUS OPERATION SPEED

Speed (r/min)	12	60	120	1000
VSD-PLL	±3.2°	±2.6°	±1.3°	±0.2°
SRF-PLL	±8.6°	±5.6°	±4.3°	±0.5°
DTMCCF-PLL	±7.1°	±5.5°	±4.7°	±0.5°

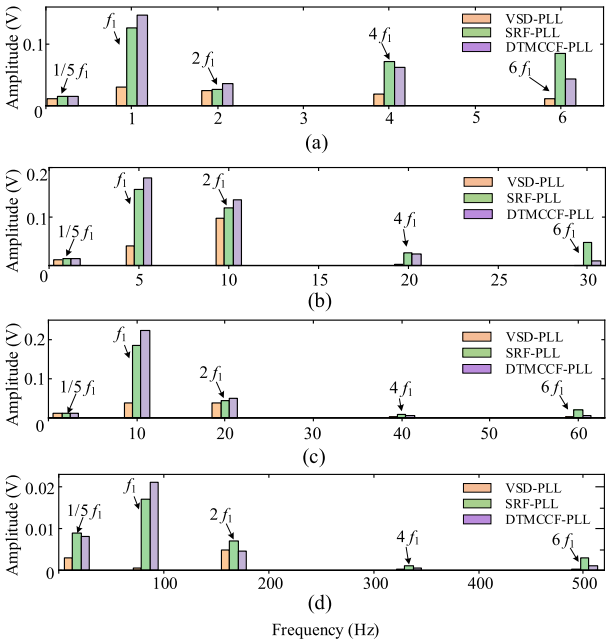

Fig. 8. FFT results of the angle error in Fig. 7 under various operation speeds: (a) 12 ($f_1 = 1$ Hz), (b) 60 ($f_1 = 5$ Hz), (c) 120 ($f_1 = 10$ Hz), and (d) 1000 r/min ($f_1 = 83.33$ Hz).

1) The estimated angle error of the three methods all contain (1/5)th harmonic, which is caused by rotor eccentricity.
2) The 4th and 6th harmonic components in angle error are caused by 5th harmonic component in linear Hall signals. As shown in Fig. 8, the 4th and 6th harmonic components can be suppressed by VSD-PLL at all-speed regions. The DTMCCF-PLL can eliminate the 4th and 6th harmonic components at the medium-high-speed regions but shows poor harmonic rejection ability at the low-speed regions.
3) Generally, there is a dc deviation in linear Hall signals resulting in dc error in $\boldsymbol{U}_{\alpha\beta}$, which introduces a fundamental frequency component in the estimated angle error, as shown in Fig. 8. According to the amplitude–frequency characteristic of the DT-MCCF [5], the dc error in $\boldsymbol{U}_{\alpha\beta}$ is amplified by DT-MCCF, which results in a larger fundamental frequency component in the estimated angle error. In contrast, the fundamental frequency component in the angle error can be suppressed by VSD-PLL.
4) The amplitude/phase unbalance introduces a negative sequence fundamental component in $\boldsymbol{U}_{\alpha\beta}$, which results in 2nd harmonic component in angle error, as shown in Fig. 8. When the motor is under low speed, the frequency difference between the negative sequence component and the positive sequence component of the fundamental frequency is small. Meanwhile, the basic frequency of the DT-MCCF is obtained from SRF-PLL, resulting in the basic frequency is not always precise due to speed ripple. Therefore, the suppression ability over the negative sequence fundamental component of DT-MCCF becomes ineffective at the low-speed regions, which results in a larger 2nd harmonic angle error. Moreover, the VSD-PLL has poor rejection ability over amplitude/phase unbalance.

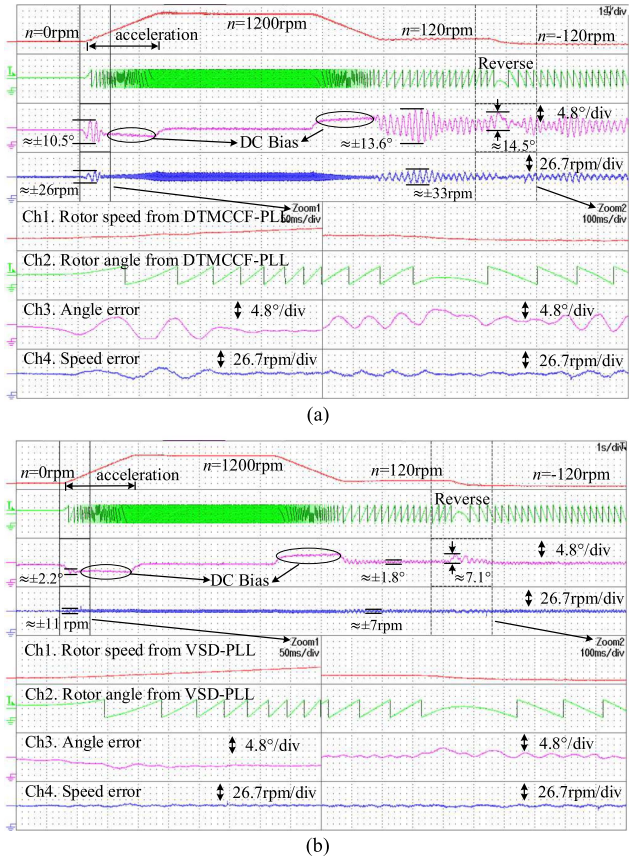

Fig. 9. Dynamic experimental results. (a) DTMCCF-PLL. (b) VSD-PLL.

C. Performance Comparisons Under Dynamic State

In this section, the motor is tested under dynamic conditions by the FOC algorithm, in which the DTMCCF-PLL [5] and VSD-PLL are utilized as the angle/speed feedback module respectively.

For DTMCCF-PLL, details about the start-acceleration region are zoomed in Fig. 9(a) Zoom1 and the reverse region is zoomed in Fig. 9(a) Zoom2. It can be found that the motor can successfully start and achieve positive-reverse operation. However, the estimated angle/speed error is very large at low-speed and standstill regions, where the angle/speed error maximum reaches ±13.6°/±33 r/min under $n = 120$ r/min and the angle error reaches 14.5° around 0 r/min. Besides, when the motor decelerates from 1200 to 120 r/min, the rotor speed estimated from DTMCCF-PLL goes through a period of oscillation before it becomes stable.

The dynamic experimental results of VSD-PLL are depicted in Fig. 9(b), which shows that the motor can successfully start

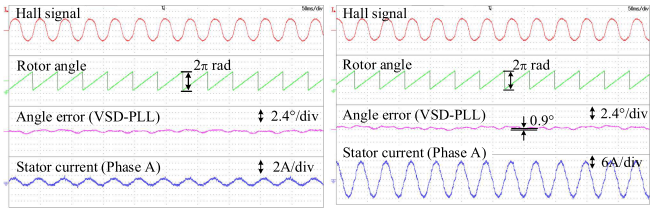

Fig. 10. Experimental results under different load conditions. (a) $I_A = 1.5$ A (no-load). (b) $I_A = 18$ A (rated load).

with a small angle error and then achieves precise control at all speed regions. It can be found that the angle/speed error maximum reaches $\pm 1.8°/\pm 7$ r/min under $n = 120$ r/min and the angle error reaches 7.1° around 0 r/min, which is much smaller compared to DTMCCF-PLL. Notably, when the motor is under acceleration, the estimated angle exists as a static error, which is attributed to the insufficient order of type-2 SRF-PLL, and the details are already discussed in [13].

D. On-Load Experiment

In the on-load experiment, the motor is controlled based on the id = 0 type FOC algorithm, where VSD-PLL is utilized as an angle/speed feedback module. When the motor rotates at $n = 300$ r/min, the amplitude of the no-load current is $I_A = 1.5$ A. Then, the adjustable load is gradually increased to $I_A = 18$ A and the experimental results are shown in Fig. 10. It can be found that the phase delay of the estimated angle between the no-load condition and the rated load condition is approximately 0.9°. In fact, the armature reaction leads to the phase shift in original linear Hall signals [12], which can be compensated. Besides, the effectiveness of harmonic suppression in VSD-PLL is still proved under on-load conditions.

IV. Conclusion

In this letter, a DTP-EME system is proposed, in which six linear Hall sensors are installed at stator slots at intervals of $(6k\pm1)\ \pi/6$ ($k = 1,2$) elec. rad. Then, a simple VSD-PLL-based rotor angle detection method is proposed to eliminate the harmonic disturbance without adding any cumbersome prefilter. This novel algorithm achieves more precise angle estimation at all-speed regions, compared with conventional SRF-PLL and prefilter-based SRF-PLL. The excellent static and dynamic performance of the proposed method was validated by experiments. Noteworthily, the 2nd harmonic component in the angle error caused by commonly existing amplitude/phase unbalance cannot be suppressed by VSD-PLL. Therefore, the effect and solution of amplitude/phase unbalance of the DTP Hall signal on rotor angle estimation is worthy of further study.

References

[1] D. Reigosa, D. Fernandez, C. González, S. B. Lee, and F. Briz, "Permanent magnet synchronous machine drive control using analog Hall-effect sensors," *IEEE Trans. Ind. Appl.*, vol. 54, no. 3, pp. 2358–2369, May/Jun. 2018.

[2] S.-T. Lee, Y.-K. Kim, and J. Hur, "Pseudo-sensorless control of PMSM with linear Hall-effect sensor," in *Proc. IEEE Energy Convers. Congr. Expo.*, 2017, pp. 1896–1900.

[3] S.-Y. Jung and K. Nam, "PMSM control based on edge-field Hall sensor signals through ANF-PLL processing," *IEEE Trans. Ind. Electron.*, vol. 58, no. 11, pp. 5121–5129, Nov. 2011.

[4] X. Song, J. Fang, and B. Han, "High-precision rotor position detection for high-speed surface PMSM drive based on linear Hall-effect sensors," *IEEE Trans. Power Electron.*, vol. 31, no. 7, pp. 4720–4731, Jul. 2016.

[5] Y. Wang, W. Hua, C. Zhang, Z. Wu, and H. Zhang, "Concept and implementation of embedded magnetic encoder in flux-switching permanent-magnet machines," *IEEE Trans. Ind. Electron.*, vol. 69, no. 11, pp. 11796–11806, Nov. 2022.

[6] Y. Wang et al., "Implementation of embedded magnetic encoder for rotor position detection based on arbitrary phase-shift phase-lock loop," *IEEE Trans. Ind. Electron.*, vol. 69, no. 2, pp. 2033–2043, Feb. 2022.

[7] Z. Q. Zhu, Y. F. Shi, and D. Howe, "Rotor position sensing in brushless AC motors with self-shielding magnets using linear Hall sensors," *J. Appl. Phys.*, vol. 99, no. 8, Apr. 2006, Art. no. 08R313.

[8] Y. Shi, H. Li, and B. Han, "Position extraction of ultralow-speed gimbal servo system with linear Hall sensors," *IEEE Trans. Ind. Electron.*, vol. 69, no. 3, pp. 2947–2955, Mar. 2022.

[9] X. Guo, W. Wu, and Z. Chen, "Multiple-complex coefficient-filter-based phase-locked loop and synchronization technique for three-phase grid interfaced converters in distributed utility networks," *IEEE Trans. Ind. Electron.*, vol. 58, no. 4, pp. 1194–1204, Apr. 2011.

[10] Y. Zhao and T. A. Lipo, "Space vector PWM control of dual three-phase induction machine using vector space decomposition," *IEEE Trans. Ind. Appl.*, vol. 31, no. 5, pp. 1100–1109, Sep./Oct. 1995.

[11] J. Malvar et al., "Graphical diagram for subspace and sequence identification of time harmonics in symmetrical multiphase machines," *IEEE Trans. Ind. Electron.*, vol. 61, no. 1, pp. 29–42, Jan. 2014.

[12] C. Zhang, Y. Wang, H. Zhang, Z. Wu, J. Tao, and W. Hua, "Armature reaction on implementation of embedded magnetic encoder in fractional-slot concentrated-winding permanent magnet machines," *IEEE Trans. Ind. Electron.*, vol. 70, no. 7, pp. 6699–6710, Jul. 2023.

[13] S. Golestan, M. Monfared, F. D. Freijedo, and J. M. Guerrero, "Advantages and challenges of a type-3 PLL," *IEEE Trans. Power Electron.*, vol. 28, no. 11, pp. 4985–4997, Nov. 2013.